DESIGN AND ANALYSIS OF AN AEROELASTIC VALIDATION EXPERIMENT FOR MOVING FLEXIBLE AIRFOILS

R. Unger*, J. Kleinert*, M.C. Haupt*, P. Horst*

J. Windte†, S. Bansmer†, C.J. Kähler†, R. Radespiel†

*Institute of Aircraft Design and Lightweight Structures, Technische Universität Braunschweig
Hermann-Blenk-Str. 35, D-38108 Braunschweig

†Institute of Fluid Mechanics, Technische Universität Braunschweig
Bienroder Weg 3, D-38106 Braunschweig

Germany

Abstract

This paper describes the aerodynamic and structural design of an airfoil, which is inspired by bird's flapping flight and can be used technically for micro-air vehicles in a low flight speed regime. Due to the high flexibility of the airfoil, a multidisciplinary design approach is conducted here. First flow measurements using the rigid version of the airfoil are presented and the experimental setup using the Particle Image Velocimetry (PIV) is shown. Further, different structural designs are discussed and computational elements to treat the coupled system, which is defined due to the fluid and structural interaction phenomena. These elements are used to calculate the unloaded shape of the airfoil (jig-shape) and to employ first unsteady, coupled computations.

1 INDRODUCTION

To increase the performance and flight speed range as well as to extend the area of application for future micro air vehicles in the low speed flow domain, the usage of biomimetic effects, inspired by flapping bird wing flight, is an attractive approach. While rigid wings of modern aircraft use disjoint systems for lift and thrust generation, both forces can be produced by the application of flexible wings. Thereby the stiffness and density distribution has a major influence on the performance and efficiency of the wing, i.e. on thrust, lift and drag.

To analyze the aeroelastic effects, the design as well as the experimental and numerical analysis of an oscillating airfoil is described in this contribution. The high qualitative flow measurements are carried out by the aid of the Particle Image Velocimetry (PIV), where laminar separation bubbles and dynamic flow separation needs to be considered. Due to the interaction effects, the wing has to be designed in a multidisciplinary procedure. First the airfoil shape for low speed range and low Reynolds numbers based on a hand foil of a seagull is designed, followed by the structural design, whereby the structure has to be flexible and lightweight. The structural model is constructed for a wind tunnel investigation, where a combined and harmonic flapping and pitching movement with a frequency of $3-6\,\mathrm{Hz}$ is aerodynamically and structurally investigated. Thereby, the trailing edge undergoes a deformation of approximately $5-10\,\%$ of the chord length.

In this paper, the design of the aerodynamic shape as well as the structural system will be shown in detail. First results of wind tunnel experiments using PIV and numerical results from the steady design process will be given and first results from the unsteady aeroelastic analyses of the coupled system will be presented.

The remainder of the paper is organized as follows: in section 2 the aerodynamic design of the airfoil is presented, while in section 3 the experimental setup and first PIV results of the rigid airfoil are given. In section 4 the design of the structural subsystem is described and in section 5 the computational elements used for coupled analysis are explained. Finally in section 6 first steady and unsteady results from coupled computations are shown.

2 AERODYNAMIC AIRFOIL DESIGN

2.1 General Considerations

In 1970, OEHME presented a study about gauging airfoils of various bird species [1]. One example, those of Passer domesticus, the house sparrow, is depicted in Fig. 1.

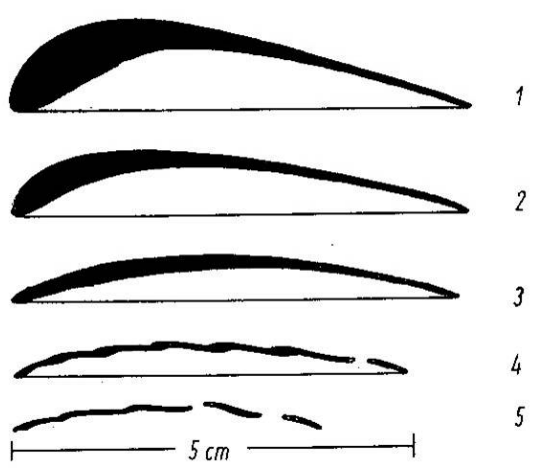

FIG. 1: Airfoil shapes of Passer domesticus at different positions of half wing span [1]

Herein, three important observations have to be remarked. First, the maximum airfoil thickness is located very close to the leading edge since this section covers the wing's main skeleton and muscles. The airfoil shape is slotted due to the pinion anatomy at the wing tip. Therefore, this section and its structural complexity will not be considered in the following investigations. The airfoil camber seems to be very high compared to technical airfoils and other observations. One reason that OEHME performed his study with narcotized birds. In fact, during wind tunnel experiments, NACHTIGALL found out that pigeons in gliding flight have less camber than wings of exanimate pigeons [2].

Nevertheless, the camber of bird wings is one of the governing parameters for their outstanding flight performance. The camber of Passer domesticus for example changes its value from 6% up to 10% during one flapping downstroke [3]. Up to present time, it is not known exactly, if this mechanism is proceeded actively by muscle contractions or passively by means of biostructural circumstances.

2.2 Design of the SG04 airfoil

SG 04, the name of the designed airfoil, has its origins by a study of LIU [4] who determined among others airfoil shapes of seagulls using a three dimensional laser scanner. Hence, seagull's wing geometry was given in parametric style and an airfoil at 75% of half of wing span with a camber of 4% could be generated.

Based upon the original data of LIU, the following procedures were conducted with the XFOIL code [5] at Reynolds number $\mathrm{Re} = 10^5$. To calculate the transition onset, the e^N method with $N = 9$ was applied. First, an analysis serves as a parametric study to determine a favorable position of maximum camber.

As illustrated in Fig. 2, the LoD curves of the orig-

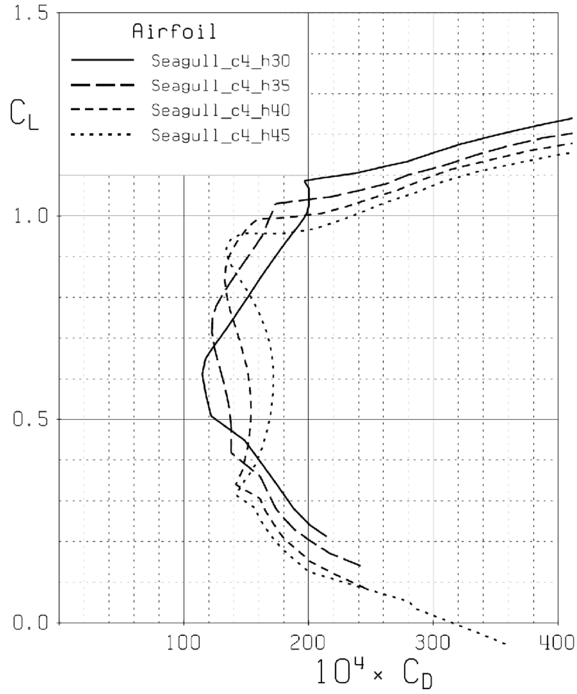

FIG. 2: Lift over drag coefficients for original seagull airfoil of LIU with variation of position of maximum camber (30%, 35%, 40% and 45%)

inal seagull airfoil given by LIU and their laminar buckets show a high dependence towards the position of maximum camber. This is due to different sizes of laminar separation bubbles as well as different positions of transition onset.

Thereafter, a broad range of analysis of pressure distributions as well as a computation on the influence of airfoil camber was accomplished. The aim was to find a solution where the size of laminar separation bubbles remains, reasonably small. Hence, the choice was made for the model with 4% in camber and 40% in position of maximum camber.

During the next step, a so called inverse design, the airfoil performance was further increased. This was done by modifying the airfoil velocity distribution in order to reduce suction peaks and the size of laminar separation bubbles. The resulting airfoil is displayed in Fig 3.

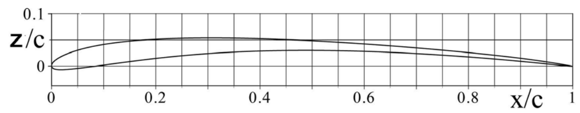

FIG. 3: Final airfoil shape of SG 04

Its new LoD curve is depicted in Fig. 4 as a solid line. Compared to the original LoD curve of LIU's airfoil in Fig. 2, the new curve is noticably smoother in its shape. Besides, the minimal drag coefficent could be decreased to $C_{D,min} = 0.015$.

Fig. 4 shows the influence of Reynolds number and

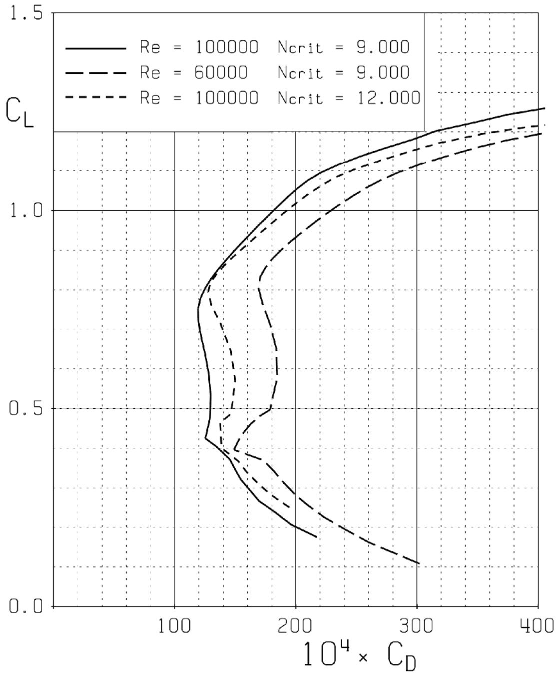

FIG. 4: Variations of the freestream flow: Reynolds number decreased to $0.6 \cdot 10^5$ or $N = N_{crit}$ increased to 12

critical N factor. Although those governing parameters of the freestream velocity field were changed*, the LoD curves remain similar on a large scale. The main difference in the curves are increased values for the drag coefficient due to larger laminar separation bubbles.

3 FIRST FLOW MEASUREMENTS OF SG04

It is one of the main goals of the project to analyze the influence of elastic flexibility on aerodynamic effects of the airfoil. To have a reference, a rigid SG 04 airfoil in composite technology was manufactured in order to consider the basic flow domain decoupled from structural wing properties. Thus, it will be possible to compare aerodynamics of the flexible wing with the results of the rigid wing in the future. Here, present first results of the flow domain of the rigid airfoil are presented, which have been gained by Particle Image Velocimetry.

3.1 Experimental Setup

The experiment was performed in the Low Noise, Low Speed Wind Tunnel (LNB) due to its relatively low turbulence level of 0.1%. The flapping flight motion apparatus was mounted around the test section as depicted in Fig. 5.

*According to empirical correlations of the flow around flat plates and other two dimensional airfoils, the critical N factor is related to the turbulence level of the freestream.

FIG. 5: Wind tunnel test section and flapping flight motion apparatus

The Flapping Flight Motion apparatus in its original configuration was already employed successfully for investigations with the SD 7003 airfoil [6]. As outlined in Fig. 6, the apparatus in its new setup is capable to perform heaving and pitching motions, which can be described in first order accuracy by the equations:

$$z(t) = \hat{z} \cdot \sin(\omega t) \tag{1}$$
$$\varphi(t) = \hat{\varphi} \cdot \sin(\omega t + \xi) + \varphi_0 \,. \tag{2}$$

Two different series of experiments were realized with the SG 04 airfoil:

1. steady conditions:

$$\begin{aligned} z(t) &= 0 \\ \varphi(t) &= \varphi_0, \text{ with } \varphi_0 = \{0°; 2°; 4°; 6°; 8°\} \\ \text{Re} &= 10^5 \end{aligned}$$

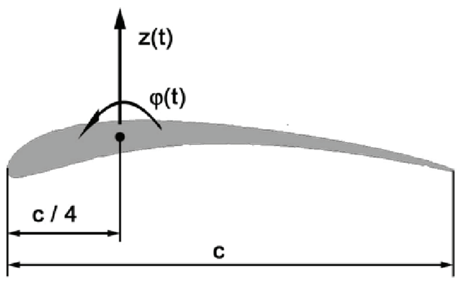

FIG. 6: Kinematics of flapping flight motion apparatus

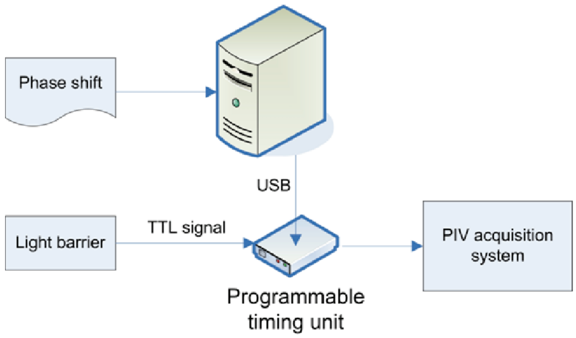

FIG. 7: Triggering of PIV acquisition system

2. unsteady conditions, pure heaving motion:

$$\begin{aligned} \hat{z} &= 10\,\text{cm} \\ \omega &= 2\pi \cdot 3.58\,\text{Hz} = 22.5\,\text{Hz} \\ \varphi(t) &= \varphi_0, \text{ with } \varphi_0 = \{0°; 2°; 4°; 6°; 8°\} \\ \text{Re} &= 10^5 \end{aligned}$$

In flapping flight, the reduced frequency k, given by:

$$k = \frac{\omega \cdot c}{2U_\infty} \tag{3}$$

is the leading parameter. The larger the reduced frequency is, the more thrust is produced. During this experiment k was set to 0.3, which corresponds to the bird flight conditions of seagulls.

A global overview of the two dimensional flow phenomena around the airfoil near the trailing edge was obtained by means of standard Particle Image Velocimetry. Air flow was seeded with oil particles ($1\,\mu$m in diameter) which were illuminated twice at different times via laser light sheet of 1 mm in thickness. Using these two particle images, the local velocity was estimated with an iterative multipass interrogation scheme with 32x32 pixel resolution and 50% in overlap. Phase locked imaging during continuous heaving motion was realized, as performed by NERGER for flapping flight experiments in a water tunnel [7]. The laser illumination and camera operation was triggered to a certain moment at each heaving cycle in order to create particle images which contain the airfoil surface always at a constant position z_{PIV}.

This was implemented using LaVision's programmable timing unit (PTU) whose operating mode is highlighted in Fig. 7. A light barrier sends at the beginning of each heaving cycle – when $z(t) = 0$ – a short impulse of rising voltage to PTU. According to a phase angle $\Delta\epsilon$ entered by computer, PTU shifts the incoming signal of light barrier to trigger the PIV acquisition system with an accuracy of $2\,\mu$s in time.

Fig. 8 shows the field of view of PIV acquisition which remained the same for all experimental series. Only the upper flow domain was of interest, the bottom side was masked out to reduce evaluation time.

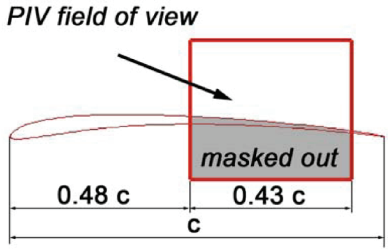

FIG. 8: PIV field of view

3.2 First PIV Results

Fig. 9 depicts a typical phase-locked particle image which was made during heaving motion experiments wit an angle of attack of $\alpha = 6°$.

The first observation in this image is clearly the reflection line of laser light sheet at the upper surface of the airfoil. Such reflections are normally not desired for PIV applications since the boundary layer is overexposed by the light. In consequence, a correlation scheme could not resolve correctly the aerodynamic phenomena there. Reducing the laser light intensity decreases the intensity of this reflection. However, the illumination of tracer particles in the flow domain decreases in same way which diminishes PIV correlation quality. Increasing the laser light intensity, on the other hand, has the advantage of better illuminated tracer particles, but experiments showed that the laser light sheet vaporized the topcoat of the airfoil.

During phase-locked imaging, it was expected that the reflection line would be always at the same location. Indeed, the analysis of particle images revealed a minimal variance of this location of about one pixel. This uncertainty is negligible compared to the size of the measurement volume of 32x32 px^2. Nevertheless, it is the objective for upcoming stereo PIV measurements to increase this acquisition accuracy to subpixel scales.

Regarding to Fig. 9, the seeding distribution itself has a good quality. Particularly, the zone near the

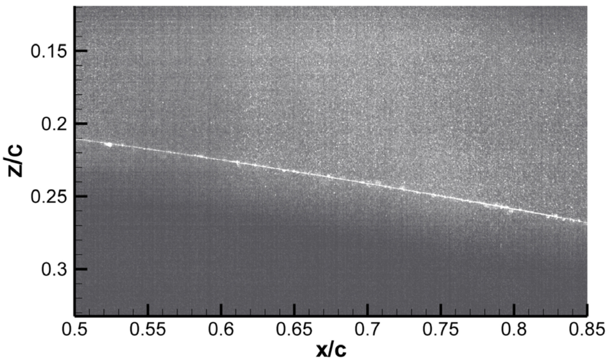

FIG. 9: Particle Image during heaving motion, $\alpha = 6°$

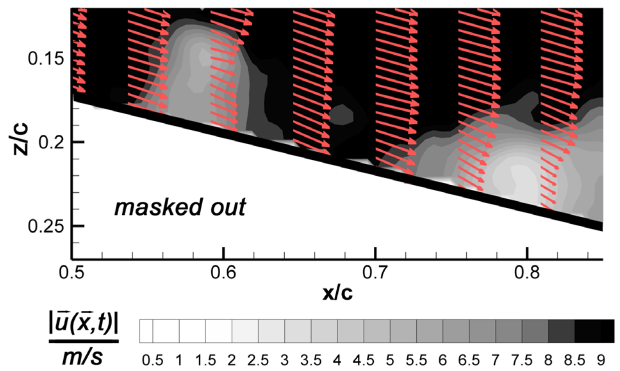

FIG. 10: PIV evaluation, instantaneous flow field, $\alpha = 6°$, phase locked image during downstroke of pure heaving motion

airfoil surface is moderately filled with at least twelve particles per interrogation window. At the bottom, the image exhibits tracer particles below the reflection line. This is caused by surface reflections and was masked out as well.

Having executed cross correlation scheme, Fig. 10 points out one example of the instantaneous flow field along the upper surface of SG 04 in pure heaving motion. The flow domain outside the boundary layer is very well represented with velocity vectors. Visibly, there are two macroscopic zones where the magnitude of the velocity field decreases significantly – indicated by light shaded areas. This could be due to downwashing vortices, however, further analysis is still required.

With this experimental setup for global flow analysis it was not possible to resolve the boundary layer. For the future, it is planned to increase spatial resolution and to capture the flow domain from different view perspectives by applying stereoscopic PIV in connection with novel evolution approaches [6]. In consequence, the phenomena in the boundary layer itself like laminar separation bubbles as they were already observed for SD 7003, will be investigated in more detail [8]. On the other hand, the interactions between boundary layer and large scale turbulent structures become more and more of interest, because theywould be the reason for the outstanding flight performances of birds.

4 STRUCTURAL DESIGN

4.1 Preanalysis

In a preanalysis, several lightweight construction methods were evaluated to find a design, which is simply to manufacture with carbon fiber reinforced plastic, Fig. 11. Inspired by a thin section of the pigeon's pinion, Fig. 11a, the design of the structural airfoil needs to fulfill flexibility and a light weight. Further, the final structural model, which is build for

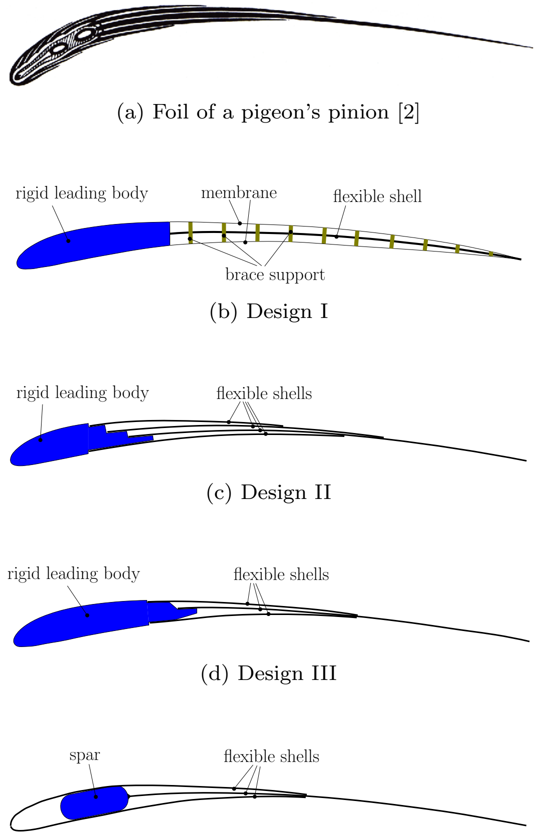

(a) Foil of a pigeon's pinion [2]

(b) Design I

(c) Design II

(d) Design III

(e) Design IV

FIG. 11: Design studies of the airfoil

wind tunnel test campaigns, should retain 2D behavior and providing a smooth surface shape. Design I, Fig. 11b, with its flexible shell, membranes and brace supports has shown to result in a heavy-weight foil and further difficulties are expected with the membranes, which needs to be mounted under high tension to get the desired flexibility of the airfoil. According to the real-life pigeon's pinion, design II, Fig. 11c, is more reliable adapting the concept of feathers. However, using more than three shells, the foil has shown to be too heavy-weighted and therefore conceptual investigations of the structure were numerically carried out with the design III, Fig. 11d, to find appropriate parameters, e.g. module of elasticity, density, etc.

The aerodynamic airfoil was used to design a structural wing with a defined span and 2D properties for the wind tunnel campaigns, Fig. 12. The rigid lead-

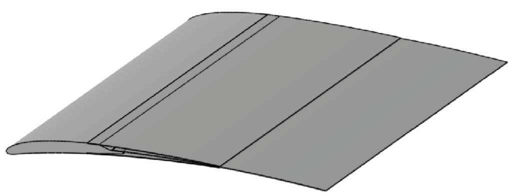

FIG. 12: Structural model

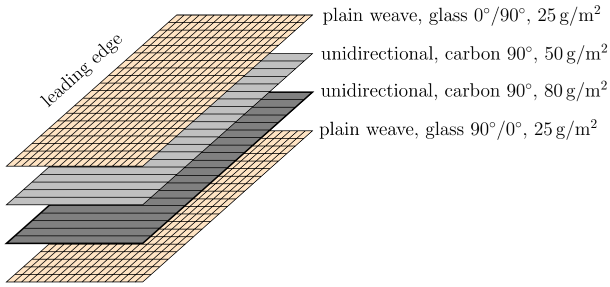

FIG. 13: Layer structure of the shells

ing part is assumed to be plastic material and the three shells are made by carbon fiber reinforced composites to emulate a natural mass and stiffness distribution. The shells are numerically investigated using the method of finite elements and varying their thickness, number of layers, layer structure and module of elasticity. Initially a pressure distribution from a stationary flow condidions with $\alpha = 3°$ obtained by XFOIL was used as a first load assumption and the deflection of the trailing edge was compared. Here it was found, that a shell thickness of 0.15 mm and a layer structure according to Fig. 13 give reasonable deflection of the trailing edge (4% of the chord length) and that the structure itself retains good 2D behavior. Further, the length of the upper and lower shell was chosen to be 50 % of the middle shell due to the minimal deflection and light weight of this configurations. Modal and harmonic analyses were performed to show the influence of the inertia loads. Here, a first eigenfrequency of approximate $8 - 10$ Hz was found, which is significant higher than the flapping frequency of tall birds ($1 - 2$ Hz).

4.2 Final Structural Design

To save more weight and due to manufacturing reasons, design III was modified to design IV, where the upper and lower shell are glued together at the leading edge, Fig. 11e. The middle shell is now jointed with a stiff spar also made by carbon fiber reinforced composites. It also should be noted here, that the upper and lower shell are prestressed to ensure all-time contact during a flapping period. The structural model was build and the flexibility can be seen from Fig. 14. The parameters for the model are summarized in Tab. 1.

Further, the final shape of the structural airfoil is designed in a way that the aerodynamic airfoil shape is obtained as the flight shape assuming gliding flight with an angle of attack of $\alpha = 3°$ and a Reynolds number of $\mathrm{Re} = 10^5$. To find the unloaded shape (jig-shape) of the structural airfoil, a finite element analysis fully coupled with an unsteady Reynolds-Averaged Navier-Stokes (URANS) flow solver [9] is utilized here, which also takes transition effects along a laminar separation bubble into account [10]. The methodology of the coupling analysis is described in the section below.

(a)

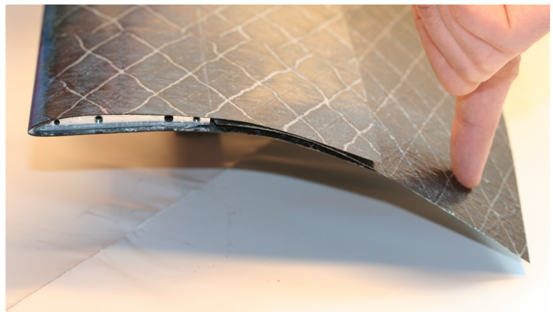

(b)

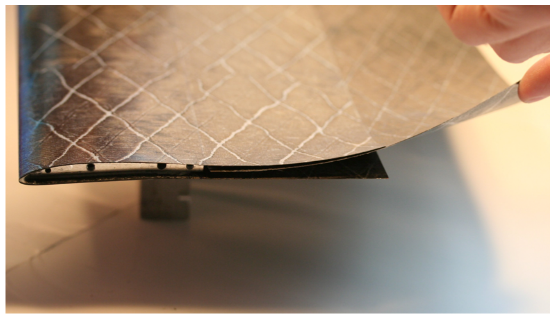

(c)

FIG. 14: Structural model of the flexible airfoil

5 COUPLING SCHEME FOR THE AEROELASTIC ANALYSIS – NUMERICAL ELEMENTS

Due to the nonlinearities, the physical system, where the structure is coupled with the flow field, is treated in the time domain. Using a well validated finite element analysis tool for the structure and a finite volume code for the fluid, three coupling aspects have to be considered for the steady and unsteady flight case; firstly the transfer of loads and states across non-matched interface discretization, secondly the mesh deformation of the fluid grid and the integration of the Arbitrary-Lagrangian-Euler (ALE) formulation into the fluid flow solver and thirdly the equilibrium iteration and time integration of the whole coupled system.

5.1 Load and State Transfer

For the state transfer across nonmatching interface grids, a weak formulation of the continuity transfer condition is used here:

$$u_s^\Gamma = u_f^\Gamma \;\rightarrow\; \int_\Gamma \lambda(u_s^\Gamma - u_f^\Gamma)\,\mathrm{d}\Gamma\,, \tag{4}$$

where u_s^Γ and u_f^Γ are the structural and fluid displacements defined on the coupling interface Γ, and λ is the Lagrange multiplier, which weights the jump of the interface state variables. The Lagrange multiplier has the physical meaning of a traction force gluing the both subdomains together.

Using a spatial discretization of the interface state variables with the aid of shape function, the Lagrange multiplier can be independently discretized under the requirements of existence and uniqueness of the solution of the formulation of Eq. (4). Therefore λ is defined on the fluid interface using a Galerkin based form, where the shape functions of the Lagrange multiplier are chosen to be the same as for the displacements of the fluid interface, Fig. 15a, and the discretized version of Eq. (4) reads:

$$\boldsymbol{M}_{ff}\boldsymbol{u}_f = \boldsymbol{M}_{fs}\boldsymbol{u}_s \quad \text{with} \quad \boldsymbol{M}_{fi} = \int_\Gamma \boldsymbol{N}_f^T \boldsymbol{N}_i \,\mathrm{d}\Gamma\,, \tag{5}$$

which has to be solved for $\boldsymbol{u}_f$. The coupling matrices are evaluated with the aid of a quadrature rule, see [11] for details. Alternatively, a collocation method can be used, where the Dirac-delta function serves as the shape function for the Lagrange multiplier, Fig. 15b. While the latter method is advantageous, because the integral of Eq. (4) vanishes and the transfer equation reduces to the evaluation of the structural shape functions at the fluid nodes, the former shows more local accuracy of the transfer condition [12].

Once the state transfer over the interface is defined, the proper load transfer is obtained straightforward, using the transposed relation of the state transfer. According to the principle of virtual work and with the schemes described above, conservation in the load is retained, which is essential for aeroelastic problems. With:

$$\delta\boldsymbol{u}_f^T\boldsymbol{f}_f = \delta\boldsymbol{u}_s^T\boldsymbol{f}_s \quad \text{and} \quad \boldsymbol{u}_f = \mathcal{T}\boldsymbol{u}_s \tag{6}$$

chord length	200 mm
half span	398 mm
shell thickness	0.15 mm
contact position of shells	65%
weight	112 g

TAB. 1: Parameters of the structural design

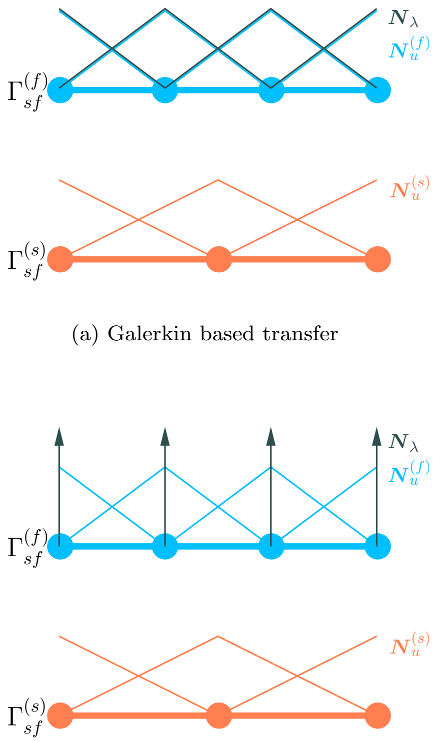

(a) Galerkin based transfer

(b) Transfer based on Dirac delta functions

FIG. 15: Transfer schemes

the load transfer is obtained as:

$$\boldsymbol{f}_s = \mathcal{T}^T\boldsymbol{f}_f\,, \tag{7}$$

where $\mathcal{T}$ is an operator which maps one variable from one grid to another. Neglecting the forces due to friction of the fluid flow and using the Galerkin based transfer, the fluid pressure distribution can directly be used for the load transfer:

$$\begin{aligned} \boldsymbol{u}_f &= \boldsymbol{M}_{ff}^{-1}\boldsymbol{M}_{fs}\boldsymbol{u}_s \\ \rightarrow \boldsymbol{f}_s &= \boldsymbol{M}_{fs}^T\boldsymbol{M}_{ff}^{-1}\boldsymbol{f}_f = \boldsymbol{M}_{fs}^T\boldsymbol{p}_f\,. \end{aligned} \tag{8}$$

5.2 Grid Deformation

For the deformation of the fluid grid, the mesh is treated as a pseudo structural system and the fluid interface displacements are applied as Dirichlet boundary conditions, see also [13]:

$$\begin{bmatrix} \boldsymbol{K}_{\Omega\Omega}^f & \boldsymbol{K}_{\Omega\Gamma}^f \\ \boldsymbol{K}_{\Gamma\Omega}^f & \boldsymbol{K}_{\Gamma\Gamma}^f \end{bmatrix} \begin{bmatrix} \boldsymbol{u}_\Omega^f \\ \boldsymbol{u}_\Gamma^f \end{bmatrix} = \begin{bmatrix} \boldsymbol{0} \\ \boldsymbol{0} \end{bmatrix}. \tag{9}$$

This equation has to be solved for $\boldsymbol{u}_\Omega^f$ and as an abbreviation the mesh deformation is written as:

$$\boldsymbol{u}^f = \mathcal{G}(\boldsymbol{u}_\Gamma^f)\,. \tag{10}$$

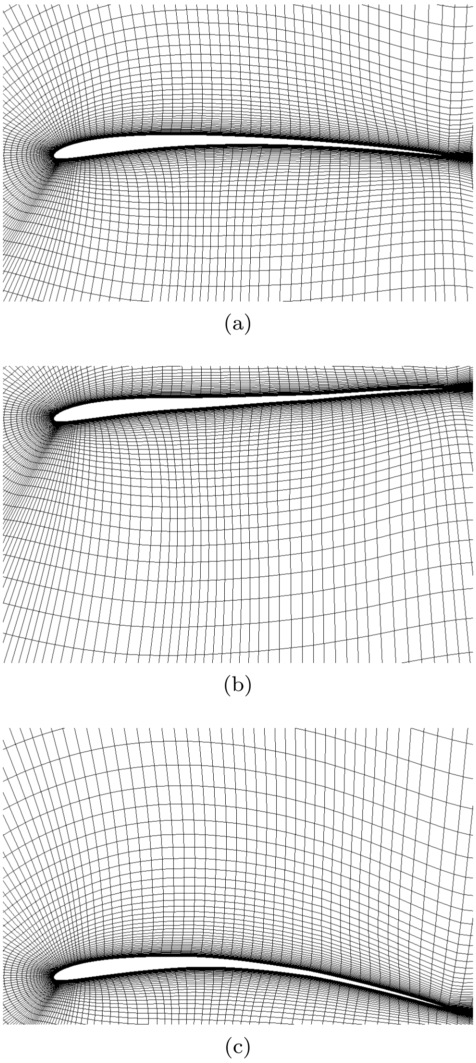

FIG. 16: Grid deformation

Here an adaptive pseudo stiffness of the mesh is used, which values depends on the local geometric dimensions within the mesh:

$$E_i^f = \frac{1}{\min(x_{i,s})}; \quad s = 1, .., 4\,, \tag{11}$$

where E_i^f is the module of elasticity for the cell i and $x_{i,s}$ is the length of the edge s in the cell i. Therefore smaller cells near the wall have a higher stiffness than greater cells in the farfield. This approach results in deformed grids with better convergence properties with respect to the fluid solver. Examples of the grid deformation including rigid body motion are depicted in Fig. 16.

This grid deformation can be used in conjunction with the flow solver which solves the unsteady Reynolds-Averaged Navier-Stokes equation on flexible block-structured grids including transition effects.

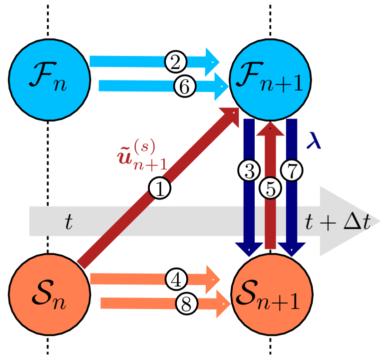

FIG. 17: Time integration scheme

5.3 Equilibrium Interation and Time Integration

Due to the use of a partitioned solution procedure, the nonlinear coupled system is solved by an iterative solution procedure. Utilizing a fluid solver, which solves the fluid equations on a given fluid grid configuration to get the fluid force on the interface:

$$\boldsymbol{f}_\Gamma^f = \mathcal{F}(\boldsymbol{u}^f) \tag{12}$$

and a structural solver, which solves the structural equation by the aid of the nonlinear finite elements method to get the structural displacements on the interface from prescribed nodal forces:

$$\boldsymbol{u}_\Gamma^s = \mathcal{S}(\boldsymbol{f}_\Gamma^s) \tag{13}$$

the defect $\boldsymbol{d}_\Gamma^s$ from the current structural displacement vector to an updated one can generally be written as:

$$\boldsymbol{d}_\Gamma^s = (\mathcal{S} \circ \mathcal{T}^T \circ \mathcal{F} \circ \mathcal{G} \circ \mathcal{T})\boldsymbol{u}_\Gamma^s - \boldsymbol{u}_\Gamma^s\,. \tag{14}$$

Eq. (14) represents the classical Dirichlet-Neumann step, where the structural interface state is transferred to the fluid side, followed by the mesh deformation and solving the fluid problem, followed by the load transfer and solving the structural problem to get a new structural interface state. The defect can be used in a relaxation step to update the problem iteratively:

$$\boldsymbol{u}_{\Gamma,k+1}^s = \boldsymbol{u}_{\Gamma,k}^s + \omega \boldsymbol{d}_{\Gamma,k}^s\,, \tag{15}$$

where ω is the relaxation parameter, which can be user-defined or calculated by the Aitken-method [15]. Alternatively, the defect can be used in a Newton-GMRES algorithm, see [16] for more details.

For transient analysis, the equilibrium iteration described above has to be carried out in every time step to advance the solution from time t to $t + \Delta t$ (time level n to $n + 1$). In Fig. 17 a schematic view of the time integration scheme is depicted, while in step 1 a predictor for the next time level is used to reduce the iteration number [17, 18]. Setting $\omega = 1$ and the

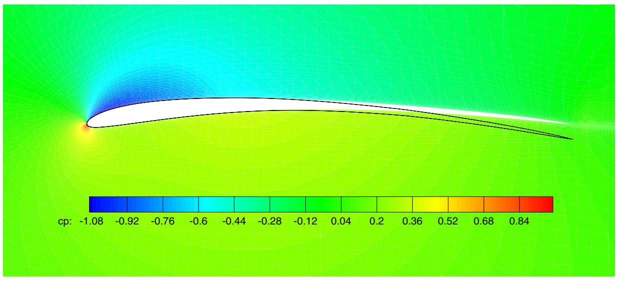

FIG. 18: Pressure contours in gliding flight (Re $= 10^5$, $\alpha = 3°$) and the jig-shape of the airfoil

maximum number of iteration during a time step to one, the so called loose coupling scheme is obtained [13].

The data transfer as well as calling of the fluid and structural analysis codes is integrated in a flexible software environment, which provides a user-friendly simulation workspace for the computation of aeroelastic fluid structure interactions, see [19] for details.

6 FIRST NUMERICAL RESULTS

With the described numerical elements, steady and unsteady computations were carried out.

6.1 Steady Analyses

To obtain the airfoil SG 04 in the flight regime of Re $= 10^5$ and $\alpha = 3°$, the unloaded shape (jig-shape) of the structure is calculated. The iteration procedure is similar to that presented in Eq. (14) unless the defect is taken compared to the original SG 04.

In Fig. 18 the jig-shape is depicted as the black boundary while the pressure distribution is calculated as steady state solution, which is similar to the one obtained by XFOIL on the surface. The used 3D structural grid is depicted in Fig. 19. The displacements of the trailing edge is calculated as 7 mm (4% of chord length).

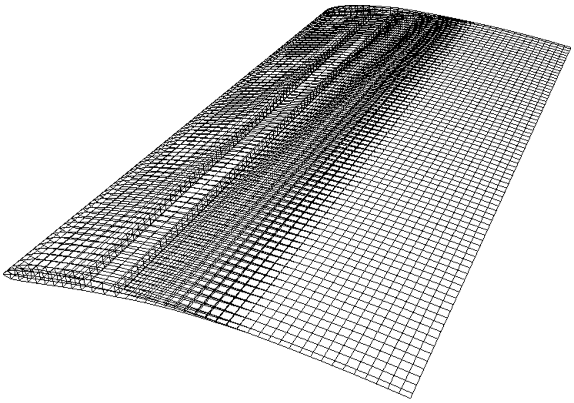

FIG. 19: Structural grid

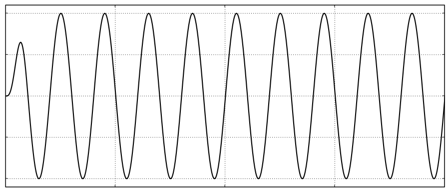

FIG. 20: Prescribed motion

6.2 Unsteady Analyses

As a first unsteady analysis the pure heaving motion ($\hat{\varphi} = \varphi_0 = 0$) of the airfoil with a frequency of $f = 5\,\mathrm{Hz}$ and an amplitude of $\hat{z} = 10\,\mathrm{cm}$ is considered. In Fig. 20 the prescribed motion of the airfoil is shown, where the steady state solution serves as the initial condition for the transient analysis and at the time $t = 0\,\mathrm{s}$ the velocity of the airfoil is set to zero. For these first calculations the loose coupling approach is used and in Fig. 21 the deflection of the airfoil and the pressure ditribution during the downstroke ($z(t) = 0$) is depicted. The displacements of the trailing edge is calculated to 33 mm (16.5% of chord length). Further computational investigations need to be performed varying the motion parameters and using a full iterative coupling scheme due to the high interaction of the fluid and the structure.

7 SUMMARY AND CONCLUSION

In this paper, the aerodynamic as well as the structural design of an airfoil inspired by biomemetics effect have been presented. The aerodynamic design of the airfoil has shown, that an airfoil with 4% and camber 40% in position of the maximum camber give appropriate behavior for the desired flight Reynolds number of Re $= 10^5$. Further first PIV results have been presented, where arising problems were discussed in detail. On the structural side the evolution of the design process has been shown to obtain an airfoil, which is lightweight, flexible and which has a natural stiffness. First numerical steady computations were employed to calculate the jig-shape of

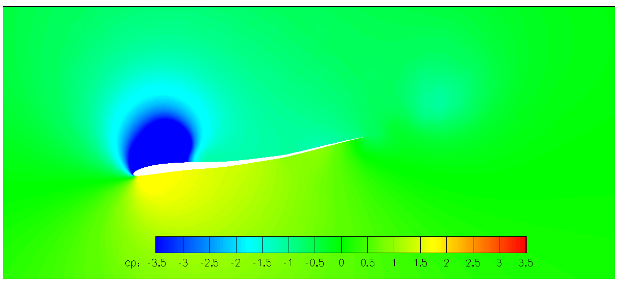

FIG. 21: Pressure distribution during the downstroke (Re $= 10^5$, $\alpha = 3°$, $z(t) = 0$)

the airfoil, and first unsteady simulations were performed, which has shown a promissing and flexible behavior of the coupled system.

ACKNOWLEDGEMENTS

The work, presented in this contribution is funded by the German Research Foundation (DFG) as part of the priority program SPP 1207.

References

[1] H. Oehme; Vergleichende Profiluntersuchungen an Vogelflügeln; 1970, Beiträge zur Vogelkunde, Band 16, Heft 1/6

[2] W. Nachtigall; Erste Messungen der Flügelgeometrie bei frei gleitfliegenden Haustauben (Columba Livia Var. Domestica) unter Benutzung neu ausgearbeiteter Verfahren der Windkanaltechnik und der Sterophotogrammetrie; 1985, BIONA report 3

[3] D. Bilo; Flugbiophysik von Kleinvögeln; I. Kinematik und Aerodynamik des Flügelabschlags beim Haussperrling (Passer domesticus L.); 1970, Zoologisches Institut der Universität München, Dissertation

[4] T. Liu, K. Kuykendoll, R. Rhew, S. Jones; Avian Wing Geometry and Kinematics; 2006, AIAA Journal, Vol. 44, No. 5, 954–963

[5] M. Drela; XFOIL: An analysis and design system for low Reynolds number airfoils, in Low Reynolds number aerodynamics; Lecture notes in Engineering, T.J. Mueller (Ed.); 1989, Springer, New York

[6] U. Scholz; Dynamics of flow structures on heaving and pitching airfoils; 2006, 13th Int. Symp. on Appl. Laser Techniques to Fluid Mechanics, Lisbon, Portugal

[7] D. Nerger, C. Kähler, R. Radespiel; Strömungsfelduntersuchungen an einem bewegten Profil im Wasserkanal mit Lasermesstechnik (Particle Image Velocimetry); 2004, DGLR Jahrbuch, Bd. 3

[8] M. Ol et al.; Comparison of Laminar Separation Bubble Measurements on a Low Reynolds Number Airfoil in Three Facilities; 2005, AIAA-2005-5149, 35th AIAA Fluid Dynamics Conference and Exhibit, Toronto, Ontario

[9] N. Kroll, C.C. Rossow, D. Schwamborn, K. Becker, G. Heller; MEGAFLOW - A Numerical Flow Simulation Tool for Transport Aircraft Design; 2002, in Proc. 23th Interanational Congress of the Aeronautical Sciences (ICAS), Toronto, Canada, Paper No. 1105

[10] R. Radespiel, J. Windte, U. Scholz; Numerical and Experimental Flow Analysis of Moving Airfoils with Laminar Separation Bubbles; 2007, AIAA Journal, Vol. 45, No. 6, 1357-1369

[11] R. Unger, M.C. Haupt, P. Horst; Application of Lagrange Multipliers for Coupled Problems in Fluid and Structural Interactions; 2007, Computers & Structures, Vol. 85, 796–809

[12] R. Unger, M.C. Haupt, P. Horst; Application of Lagrange Multipliers for Compuational Aeroelasticity; 2006, in Proc. III European Conference on Computational Mechanics, C.A.M. Soares, J.A.C. Martins, H.C. Rodrigues (et al.) (Editors), Springer

[13] C. Farhat, K.G. van der Zee, P. Geuzaine; Provably second-order time-accurate loosely-coupled solution algorithms for transient nonlinear computational aeroelasticity; 2006 Computer Methods in Applied Mechanics and Engineering, Vol. 195, 1973–2001

[14] K. C. Park, C. A. Felippa; A Variational Principle for The Formulation of Partitioned Structural Systems; 2000, International Journal for Numerical Methods in Engineering, Vol. 47, 395–418

[15] B. Irons, R.C. Tuck; A version of the Aitken accelarator for computer implementation; 1969 International Journal for Numerical Methods in Engineering, Vol. 1, 275–277

[16] R. Unger, M.C. Haupt, P. Horst; Comparison of Iterative Solution Procedures for Fluid and Structural Interaction Problems Using Two- and Three-Field Approaches; in Computational Methods for Coupled Problems in Science and Engineering II - Coupled Problems, M. Papadrakakis, E. Oñate and B. Schrefler (Editors), 2007

[17] S. Piperno; Explicit/implicit fluid/structure staggered procedures with a structural predictor and fluid subcycling for 2D inviscid aeroelastic simulations; 1997, International Journal for Numerical Methods in Fluids, Vol. 25, 1207–1226

[18] R. Unger, M.C. Haupt, P. Horst; Coupling Techniques for Computational Nonlinear Transient Aeroelasticity; 2006 in Proc. 25th Interanational Congress of the Aeronautical Sciences (ICAS)

[19] M.C. Haupt, R. Niesner, R. Unger, P. Horst; Coupling Techniques for Thermal and Mechanical Fluid-Structure-Interactions in Aeronautics; 2005, PAMM, Vol. 5(1), 19–22